

Multipoint Aerodynamic Shape Optimization Investigations of the Common Research Model Wing

Gaetan K. W. Kenway* and Joaquim R. R. A. Martins†
University of Michigan, Ann Arbor, Michigan 48109

DOI: 10.2514/1.J054154

The aerodynamic shape optimization of wings in transonic flow is an inherently challenging problem. In addition to the high computational cost of solving the Reynolds-averaged Navier–Stokes equations, there is a complex interdependence between the cross-sectional shape, wave drag, and viscous effects. Furthermore, it is necessary to perform multipoint optimizations to ensure good performance for a range of flight conditions. The choice of which flight conditions should be considered in a multipoint optimization and how many of these should be considered is still not well understood. This paper addresses this issue by solving a series of seven benchmark optimizations developed by the AIAA Aerodynamic Optimization Discussion Group. These optimization cases include a single-point optimization, four three-point optimizations, a nine-point optimization, and a five-point optimization. The optimizations consist in minimizing the weighted drag coefficient subject to lift, moment, thickness, and volume constraints. The optimizations were performed with respect to 768 shape design variables and an angle of attack for each flight condition. The single-point optimization was able to achieve an 8.1% drag reduction relative to the initial design, but it exhibited poor off-design performance. All the optimized designs were compared using a contour plot of ML/cD to evaluate the wing performance over the complete transonic flight operating envelope. Each of the four three-point optimizations successfully mitigated the poor off-design performance of the single-point design. However, the three-point optimization with widely spaced Mach numbers yielded a much more complex ML/cD contour with two distinct local maxima. Finally, the five- and nine-point optimizations yielded similar performance and the most robust off-design performance.

I. Introduction

RECENT advances in high-performance computing have enabled the deployment of full-scale physics-based numerical simulations and optimization in academia and industry. Computational fluid dynamics (CFD) tools and numerical optimization techniques have been widely adopted to shorten design cycle times and to explore design spaces more effectively. High-fidelity methods enable engineers to perform detailed designs earlier in the design process, allowing them to better understand the design tradeoffs and to make more informed design decisions. In addition, advances in sensitivity analysis via the adjoint method [1–5] have dramatically reduced the computational effort required for aerodynamic shape optimization.

Despite more than two decades of research, we still do not fully understand which problem formulations should be used to obtain practical aerodynamic designs and the best strategies for solving aerodynamic shape optimization problems. Also, performing aerodynamic shape optimization based on the Reynolds-averaged Navier–Stokes (RANS) equations on a large grid remains a challenging task. To encourage a collective effort toward a better understanding of aerodynamic shape optimization, the Aerodynamic Design Optimization Discussion Group (ADODG) has developed a series of benchmark problems that range from two-dimensional airfoil optimization based on the Euler equations to three-dimensional wing shape optimization based on the RANS equations.‡

Presented as Paper 2015-0264 at the 53rd AIAA Aerospace Sciences Meeting, Kissimmee, FL, 5–9 January 2015; received 23 December 2014; revision received 28 May 2015; accepted for publication 30 May 2015; published online 28 December 2015. Copyright © 2015 by the authors. Published by the American Institute of Aeronautics and Astronautics, Inc., with permission. Copies of this paper may be made for personal or internal use, on condition that the copier pay the \$10.00 per-copy fee to the Copyright Clearance Center, Inc., 222 Rosewood Drive, Danvers, MA 01923; include the code 1533-385X/15 and \$10.00 in correspondence with the CCC.

*Research Investigator, Department of Aerospace Engineering. Member AIAA.

†Professor, Department of Aerospace Engineering. Associate Fellow AIAA.

‡Data available online at <https://info.aiaa.org/tac/ASG/APATC/AeroDesignOpt-DG/default.aspx> [retrieved 10 April 2015].

The results for the single-point RANS-based aerodynamic shape optimization of the Common Research Model (CRM) wing were previously presented, and optimal geometries and meshes were made publicly available [6].§ These results were obtained using the aerodynamic shape optimization framework that was previously developed [7,8], which uses gradient-based optimization together with a discrete adjoint to compute the gradients efficiently. The aerodynamic shape optimization framework has also been coupled to a structural finite element solver to enable aerostructural design optimization [9–11].

When solving the single-point aerodynamic shape optimization of the CRM wing, we studied multiple local minima. We found that they do exist, but the differences in the optimal drag coefficients and the design shape are negligible: the differences in the drag coefficients were within 0.1 counts (0.05% of the minimum drag), whereas the L_2 norms of the differences in the shape were less than 1% of the mean aerodynamic chord [6]. In addition to solving the single-point optimization problem developed by the ADODG, we solved a five-point optimization. This resulted in a much more robust aerodynamic design, as demonstrated by the evaluation of the performance of all the optimal designs in $M - C_L$ space. Finally, Lyu et al. [6] also presented a multilevel optimization technique, studied the effect of the number of design variables, and solved a version of the ADODG problem with larger thickness constraints. Other researchers presented their solutions to the single-point CRM wing optimization in the same ADODG special session at the AIAA SciTech 2014 conference [12–14].

To further explore multipoint aerodynamic shape optimization, the ADODG developed a series of six multipoint cases for the RANS-based optimization of the CRM wing. We solve all six cases in the present paper, as well as an additional case, and we compare the performance of the resulting designs by making contour plots of ML/cD . Our optimized geometries and meshes for this case are available as Supplemental Materials (Supplemental Data S1–S16) for this paper.

The numerical tools used in this work are described in Sec. II. The problem formulation, mesh, and initial geometry are described in

§Data available online at <http://mdolab.engin.umich.edu/content/aerodynamic-design-optimization-workshop> [retrieved 10 April 2015].

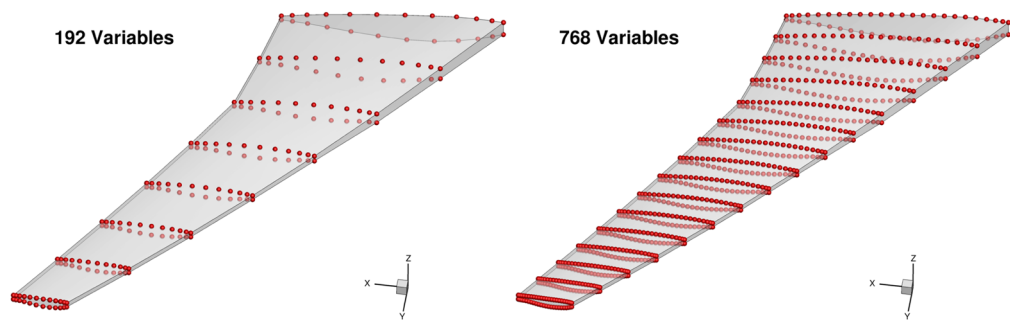


Fig. 1 Fine FFD (right) with four times the number of control points in the coarse FFD (left).

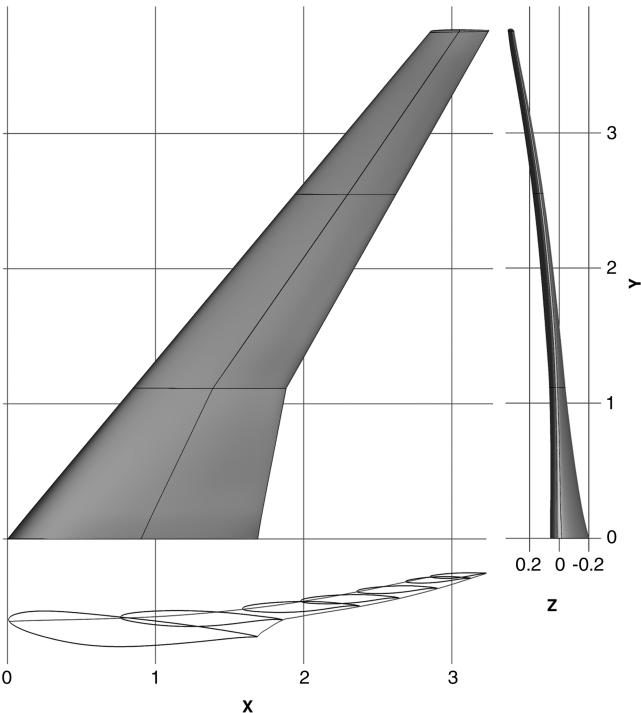


Fig. 2 Initial geometry scaled by its mean aerodynamic chord.

Sec. III. The results of the seven multipoint optimizations are presented in Sec. IV, followed by the conclusions.

II. Methodology

We now briefly describe the computational framework used for aerodynamic shape optimization. The tools used herein are a subset of the multidisciplinary design optimization of aircraft configurations with high-fidelity (MACH) framework [9,11], which has been successfully employed to solve aerodynamic design optimization [6,15–17] and aerostructural design optimization problems [9–11,18].

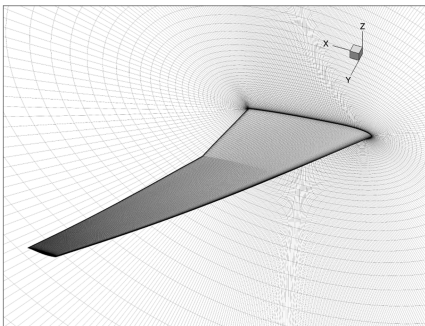
A. Geometric Parametrization

Many different geometric parameterization techniques have been successfully used for aerodynamic shape optimization. These include mesh coordinates (with smoothing) [12], B-spline surfaces [19], Hicks–Henne bump functions [20], camber-line-thickness parameterization [14], and freeform deformation (FFD) [21]. The only requirement specified by the ADODG for the parameterization is that the planform must remain fixed and changes in shape may be made only in the vertical (z) direction. All of the aforementioned techniques can satisfy these requirements if implemented correctly. In this work, we use an FFD volume approach that we implemented [21] and used extensively [16,9–11,15–18].

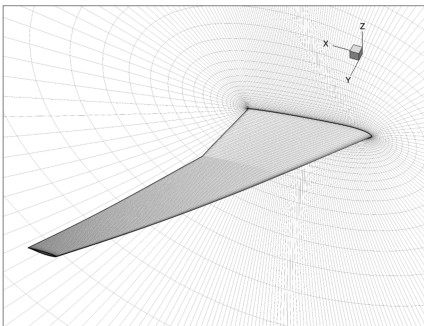
The FFD approach can be visualized as embedding the spatial coordinates defining a geometry inside a flexible volume. The parametric locations (u, v, w) corresponding to the initial geometry are found using a Newton search algorithm. Once the initial geometry

Table 1 Drag differences between the initial and optimized meshes

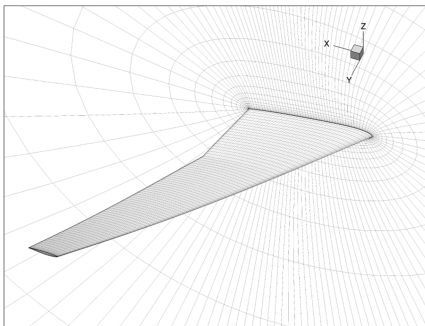
Mesh level	Chordwise cells	Spanwise cells	Offwall cells	y_{\max}^+	Total cells	Initial C_D , counts	Optimized C_D , counts	ΔC_D , counts	C_L	Optimized C_M
$h = 0$	—	—	—	—	∞	198.92	182.56	−16.36	—	—
L0	480	368	160	~ 0.5	28,835,840	199.59	183.24	−16.35	0.500	−0.169
L1	240	184	80	~ 1.0	3,604,480	201.59	185.28	−16.31	0.500	−0.170
L2	120	92	40	~ 2.2	450,560	210.99	197.03	−13.96	0.500	−0.172



a) L0 grid has 28.8 million cells



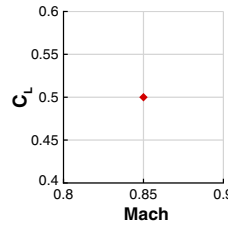
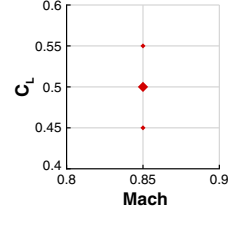
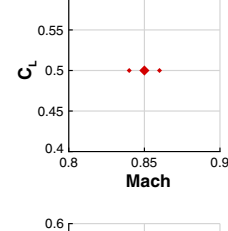
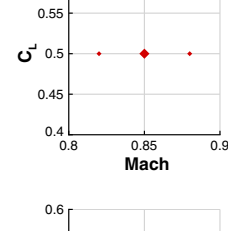
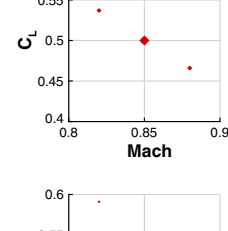
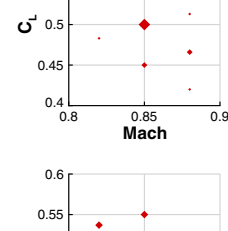
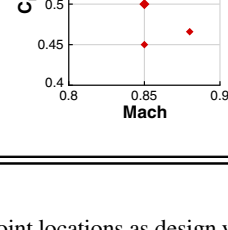
b) L1 grid has 3.6 million cells



c) L2 grid has 450,000 cells

Fig. 3 O-grids of varying sizes were generated using a hyperbolic mesh generator.

Table 2 Operating conditions for each optimization

Case	Point	Weights \mathcal{T}_i	Mach	C_L	Reynolds number	$M - C_L$ plot
4.1	1	1.0	0.85	0.500	5.00×10^6	
4.2	1	1/4	0.85	0.450	5.00×10^6	
	2	1/2	0.85	0.500	5.00×10^6	
	3	1/4	0.85	0.550	5.00×10^6	
4.3	1	1/4	0.84	0.500	5.00×10^6	
	2	1/2	0.85	0.500	5.00×10^6	
	3	1/4	0.86	0.500	5.00×10^6	
4.4	1	1/4	0.82	0.500	5.18×10^6	
	2	1/2	0.85	0.500	5.00×10^6	
	3	1/4	0.88	0.500	4.83×10^6	
4.5	1	1/4	0.82	0.537	4.82×10^6	
	2	1/2	0.85	0.500	5.00×10^6	
	3	1/4	0.88	0.466	5.18×10^6	
4.6	1	1/16	0.82	0.483	4.82×10^6	
	2	1/8	0.82	0.537	4.82×10^6	
	3	1/16	0.82	0.591	4.82×10^6	
	4	1/8	0.85	0.450	5.00×10^6	
	5	1/4	0.85	0.500	5.00×10^6	
	6	1/8	0.85	0.550	5.00×10^6	
	7	1/16	0.88	0.442	5.18×10^6	
	8	1/8	0.88	0.466	5.18×10^6	
	9	1/16	0.88	0.513	5.18×10^6	
4.7	1	3/16	0.82	0.537	4.82×10^6	
	2	3/16	0.85	0.450	5.00×10^6	
	3	1/4	0.85	0.500	5.00×10^6	
	4	3/16	0.85	0.550	5.00×10^6	
	5	3/16	0.88	0.466	5.18×10^6	

has been embedded, perturbations made to the FFD volume propagate within the embedded geometry via the evaluation of the nodes at their parametric locations. We use trivariate B-spline volumes for the FFD implementation, and we use the displacement of

the control point locations as design variables. The sensitivity of the geometric location of the geometry with respect to the control points is computed efficiently using analytic derivatives of the B-spline shape functions [22].

Two FFD volumes are used in this work. The first is a coarse FFD with 192 control points arranged in a $12 \times 8 \times 2$ pattern, corresponding to the chordwise, spanwise, and vertical directions, respectively, as shown on the left side of Fig. 1. This FFD is used for the initial optimization based on a coarse mesh (named the L2 mesh), described in Sec. IV. The second FFD is based on a finer pattern ($24 \times 16 \times 2$), shown on the right side of Fig. 1, and this FFD is used for the fine (L1) mesh optimizations. A linear least-squares minimization is used to interpolate the optimized result from the coarse FFD to the fine FFD before the optimization begins. Both FFD volumes are shown in Fig. 1.

B. Mesh Perturbation

The FFD approach just described applies deformations only to the surface mesh: that is, the part of the volume mesh that lies on the wing surface. A separate operation is performed to propagate these perturbations to the remainder of the volume mesh. Because the surface changes to the fixed planform are relatively small, a simple algebraic method based on transfinite interpolation was found to be sufficient. This method is a simplification of the more complex hybrid algebraic-linear elasticity method described by Kenway et al. [21], which can handle larger shape changes.

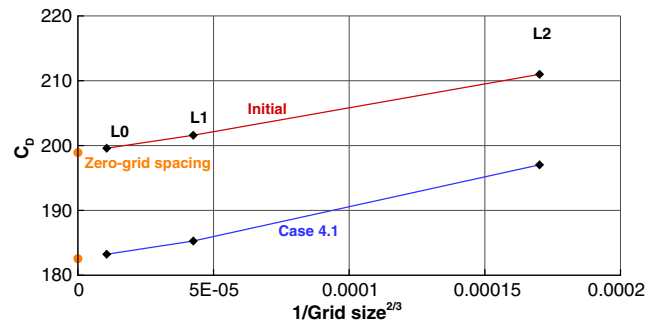


Fig. 4 Grid convergence study showing that the difference between the L1 and zero-mesh spacing value is 2.7 drag counts for the initial design.

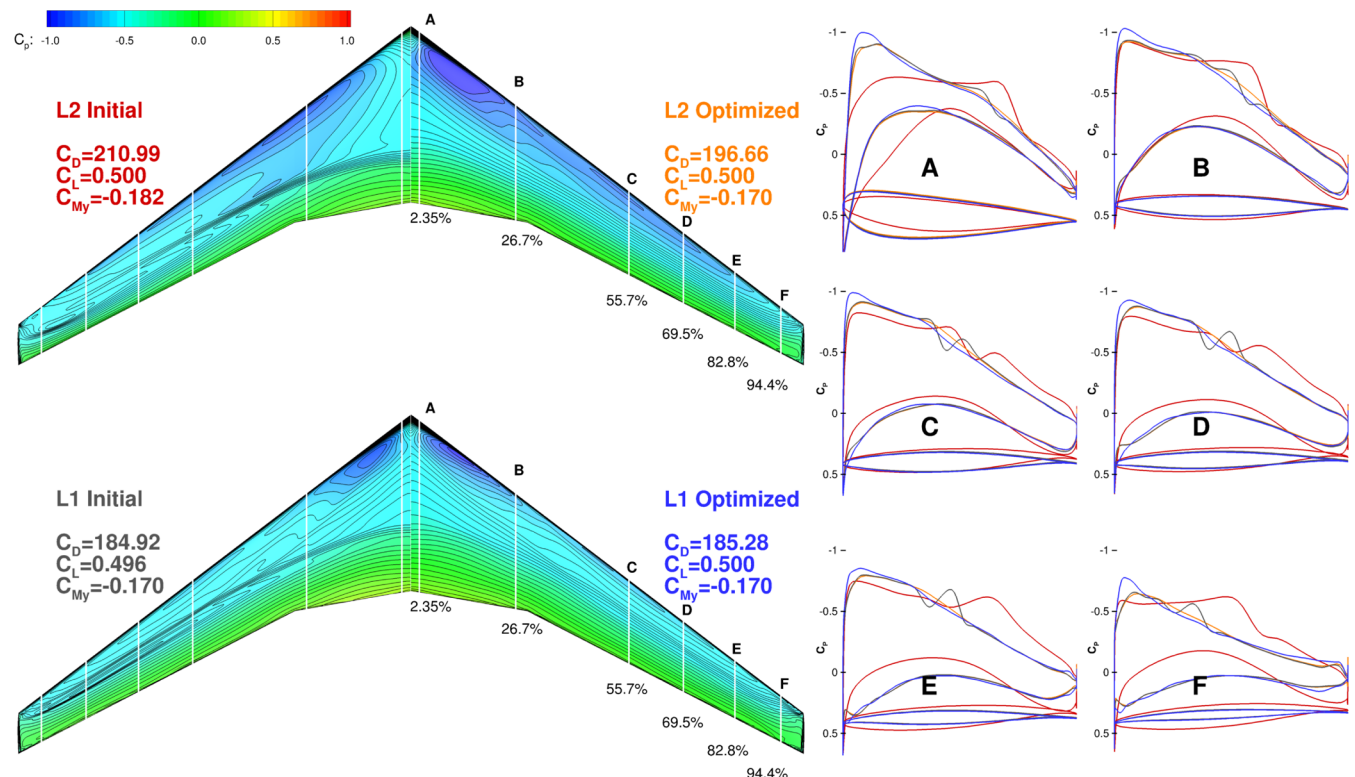


Fig. 5 The coarse grid optimum is a good starting point for the fine-grid optimization.

C. Computational Fluid Dynamics Solver

The flow solver used in this work is SUMad [23], a second-order finite volume cell-centered structured multiblock solver for the compressible RANS equations. The Jameson–Schmidt–Turkel artificial dissipation scheme [24] is employed with coefficients of $1/64$ and $1/4$ for the fourth- and second-order terms, respectively. Although this is not the most accurate dissipation scheme available, its robustness is desirable from the optimization point of view, and the hyperbolically smoothed mesh mitigates the accuracy issue, as we will see in the grid convergence study. The Spalart–Allmaras turbulence model [25] is used and, with a fully coupled Newton–Krylov method, solves the mean flow and turbulence equations simultaneously. A discrete adjoint method implemented using algorithmic differentiation is used for the efficient computation of the gradients of the functions of interest. More details on this adjoint implementation are provided by Lyu et al. [8].

D. Optimization Algorithm

The high computational cost of RANS CFD solutions dictates that the optimization must perform a reasonably low number of function calls. Some gradient-free methods, such as genetic algorithms, have a higher probability of getting close to the global minimum for cases with multiple local minima and relatively few design variables. However, as previously mentioned, our experience with the optimization of the CRM wing has failed to show significant local minima; thus, the use of gradient-based optimization is justified [6,26].

We use the sparse nonlinear optimizer (SNOPT) [27] through the Python interface pyOpt [28] for all the results presented here. SNOPT is a gradient-based optimizer that implements a sequential quadratic programming method; it is capable of solving large-scale nonlinear optimization problems with thousands of constraints and design variables. SNOPT uses an augmented Lagrangian merit function, and the Hessian of the Lagrangian is approximated using a quasi-Newton method.

III. Problem Description

The ADODG currently defines four optimization problems of increasing computational complexity (see footnote ‡):

Case 1: This optimization problem consists of a two-dimensional (2-D) Euler-based drag minimization of the NACA 0012 profile in transonic flow.

Case 2: This optimization problem consists of a 2-D RANS-based drag minimization of the RAE2822 profile in transonic flow.

Case 3: This optimization problem consists of a three-dimensional (3-D) inviscid drag minimization of the $R = 6$ wing NACA 0012 cross section in subsonic flow.

Case 4: This optimization problem consists of a 3-D RANS-based drag minimization of the CRM wing in transonic flow (single point and multipoint).

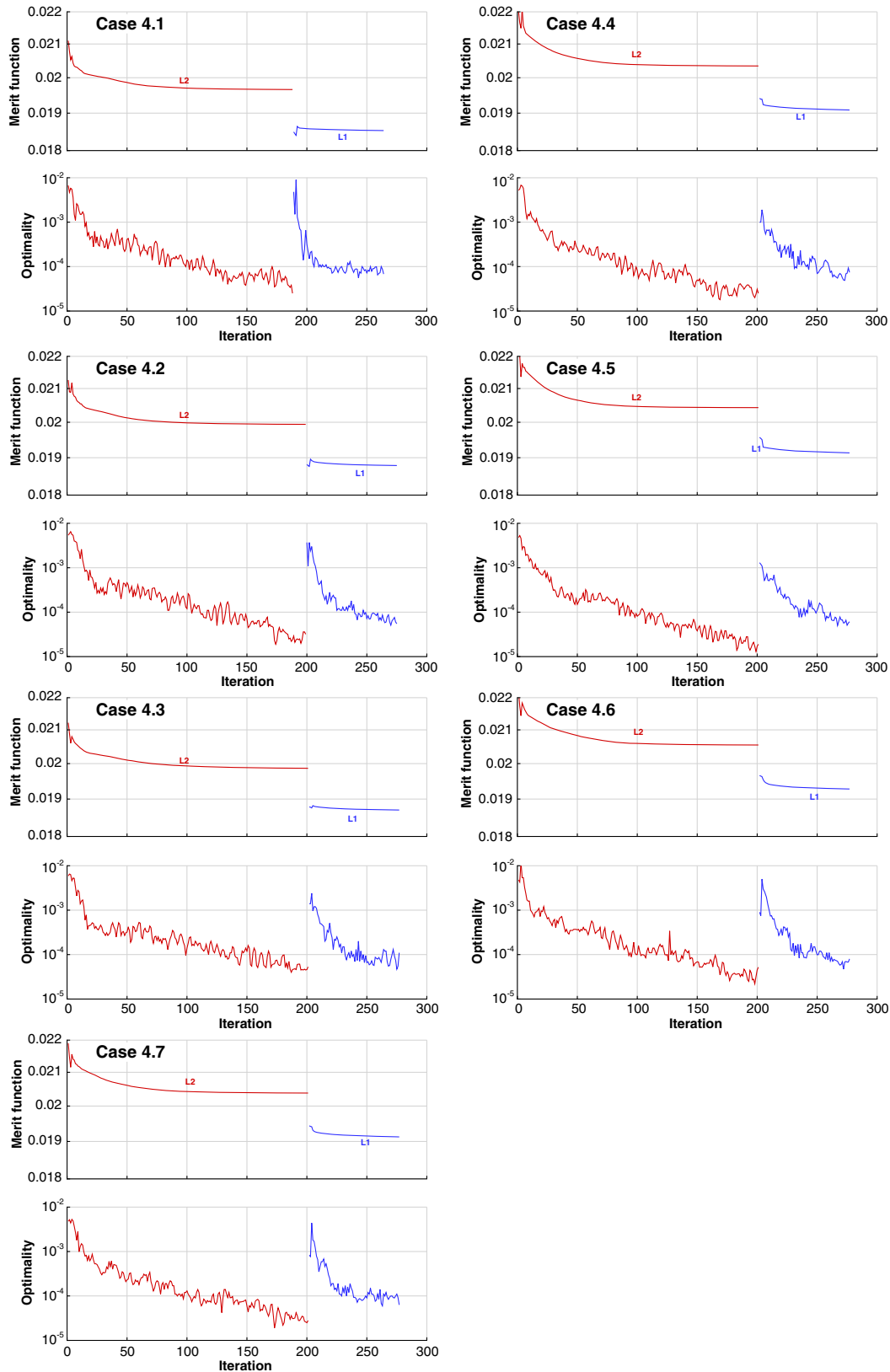


Fig. 6 Merit function and optimality evolution for each optimization case.

We focus on Case 4, which is the most physically realistic and the most demanding in terms of computational cost. Despite the increased computational cost of analyzing three-dimensional turbulent RANS flow, we have found that this case tends to be easier from an optimization perspective than when using the Euler equations because the optimization algorithm is less likely to exploit physical shortcomings of the underlying numerical model.

A. Initial Geometry

The initial geometry is a wing with a blunt trailing edge extracted from the CRM geometry. The geometry and specifications are given by the ADODG [19]. The fuselage and tail are deleted from the original CRM, and the root of the remaining wing is moved to the symmetry plane. The initial geometry is shown in Fig. 2. All the coordinates are scaled by the mean aerodynamic chord (275.8 in.). The reference wing area is 3.407014, and the point about which the pitching moment is taken is $(x, y, z) = (1.2077, 0.0, 0.007669)$.

B. Computational Grids

We generated a sequence of CFD meshes using an in-house hyperbolic mesh generator. The computational technique used in the meshing scheme follows the work of Chan and Steger [29]. The three-dimensional multiblock mesh is generated by marching a multiblock patching on the wing surface a sufficient distance away from the wing, thus automatically generating an O-type topology. For all the

cases, the far-field boundary is located at a distance of 25 times the wing semispan. We set the offwall spacing to ensure a maximum y^+ value of less than one for the L1 mesh at the nominal operating condition of $Re = 5$ million and a Mach number of 0.85.

We generated a family of three uniformly refined meshes with sizes ranging from 450,000 cells to over 28 million cells (see Table 1 for the exact numbers). The surface mesh and symmetry plane for each of the meshes are shown in Fig. 3. Only the two coarser meshes (L2 and L1) are used for optimization; the finer one (L0) is used for the grid convergence study only.

We performed a grid convergence study using the initial geometry and the optimized geometry from the single-point optimization of Case 4.1 (see Table 2 and Fig. 4). For the optimized configuration, we use the shape from the L1 optimized geometry with the L0 and L2 meshes. For this reason, the L2 drag for the optimized configuration is slightly higher than the result from the actual L2 optimization (see Fig. 4). We compute the zero-grid spacing result by extrapolating the two finest grid results, which are assumed to lie within the asymptotic convergence region. The difference between the extrapolated zero-grid spacing value and the L1 mesh is 2.7 counts (1.4%). The low slope of this grid convergence plot and the near second-order convergence indicates that the lack of wake refinement due to the O-grid is not a concern.

Given the large increase in the computational cost when optimizing with the L0 mesh, we decided that the L1 mesh was a good compromise between computational cost and fidelity [17]. This

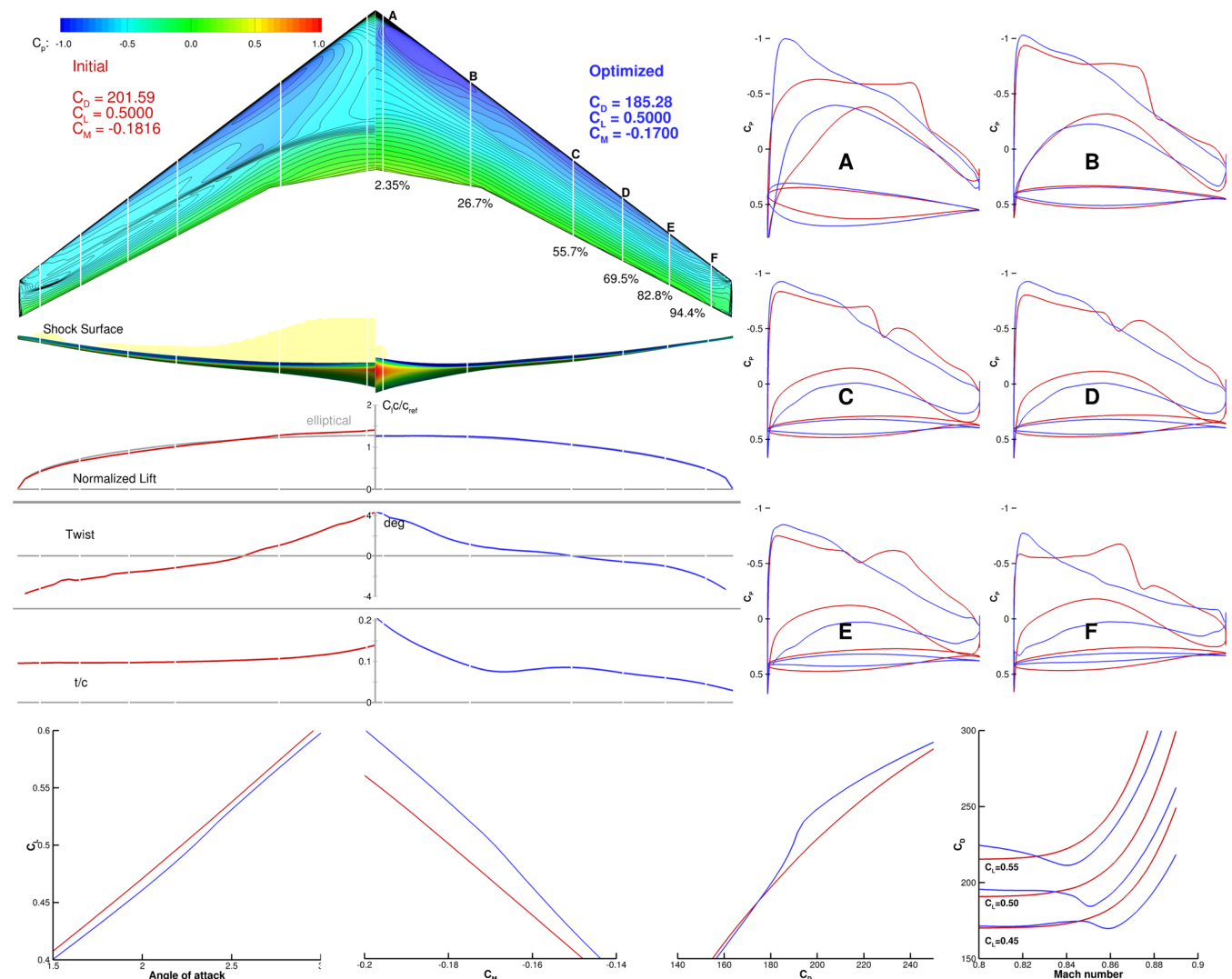


Fig. 7 Case 4.1 has the highest performing design at the nominal operating condition. The drag divergence curves show a large drop near the on-design condition.

decision is justified by the observation that the drag reductions from the single-point optimization on the L0 and L1 meshes are nearly identical. This indicates that the drag improvement predicted by the L1 mesh is entirely realized on the L0 mesh.

C. Optimization Cases

For the CRM wing geometry, the ADODG defines a total of six optimization cases. Case 4.1 is the baseline single-point optimization. Results for this case have been reported previously by the Lyu and Martins, and the resulting geometries and meshes are publicly available [17]. Cases 4.2 through 4.5 are a series of multipoint optimizations, each consisting of three different operating conditions. Various combinations of Mach number, C_L , and Reynolds number are considered. Case 4.6 is a nine-point optimization combining the operating conditions of Cases 4.2 and 4.5, with the addition of the “corners” of the resulting 3×3 pattern in $M - C_L$ space. We also add an additional problem, Case 4.7, by removing the corner points of Case 4.6. A complete description of each of the cases is given in Table 2.

The design point weights T_i for the multipoint cases 4.2 through 4.5 are derived from a one-dimensional quadrature rule and from a 2-D quadrature rule for Case 4.6. These weights correspond to performing the numerical integration of C_L over the $M - C_L$ space with a uniform continuous weighting function. This choice of weights would be logical if we valued all flight conditions equally. However, this is usually not the case, as the probability distribution over the flight condition space is nonuniform with a higher probability near the nominal flight condition [10].

To investigate if we can obtain a similar result with a lower number of points, we created Case 4.7, where we eliminate the corner points from Case 4.6, resulting in a five-point cross. The weights assigned to the four corner points are reassigned evenly to the four remaining off-design points, yielding similar weights for all flight conditions. This distribution of weights puts more relative emphasis on the nominal flight condition, around which the aircraft is more likely to fly.

The general form of each L1 optimization problem statement is shown in Table 3, where N is the number of flight conditions considered:

Table 3 Design optimization problem statement for N flight conditions

	Function/variable	Description	Quantity
minimize	$\sum_{i=1}^N T_i C_{D_i}$	Weighted average drag	
with respect to	x_{shape}	z perturbation in FFD control points	768
	α_i	Angle of attack	N
		Total design variables	$768 + N$
subject to	$C_{L_i} - C_{L_i}^* = 0$	Lift constraints	N
	$C_M \geq -0.17$	Moment constraint at nominal condition	1
	$V \geq V_{\text{init}}$	Volume constraint	1
	$t_j \geq 0.25t_{j\text{init}}$	Thickness constraints	750
		Total constraints	$752 + N$

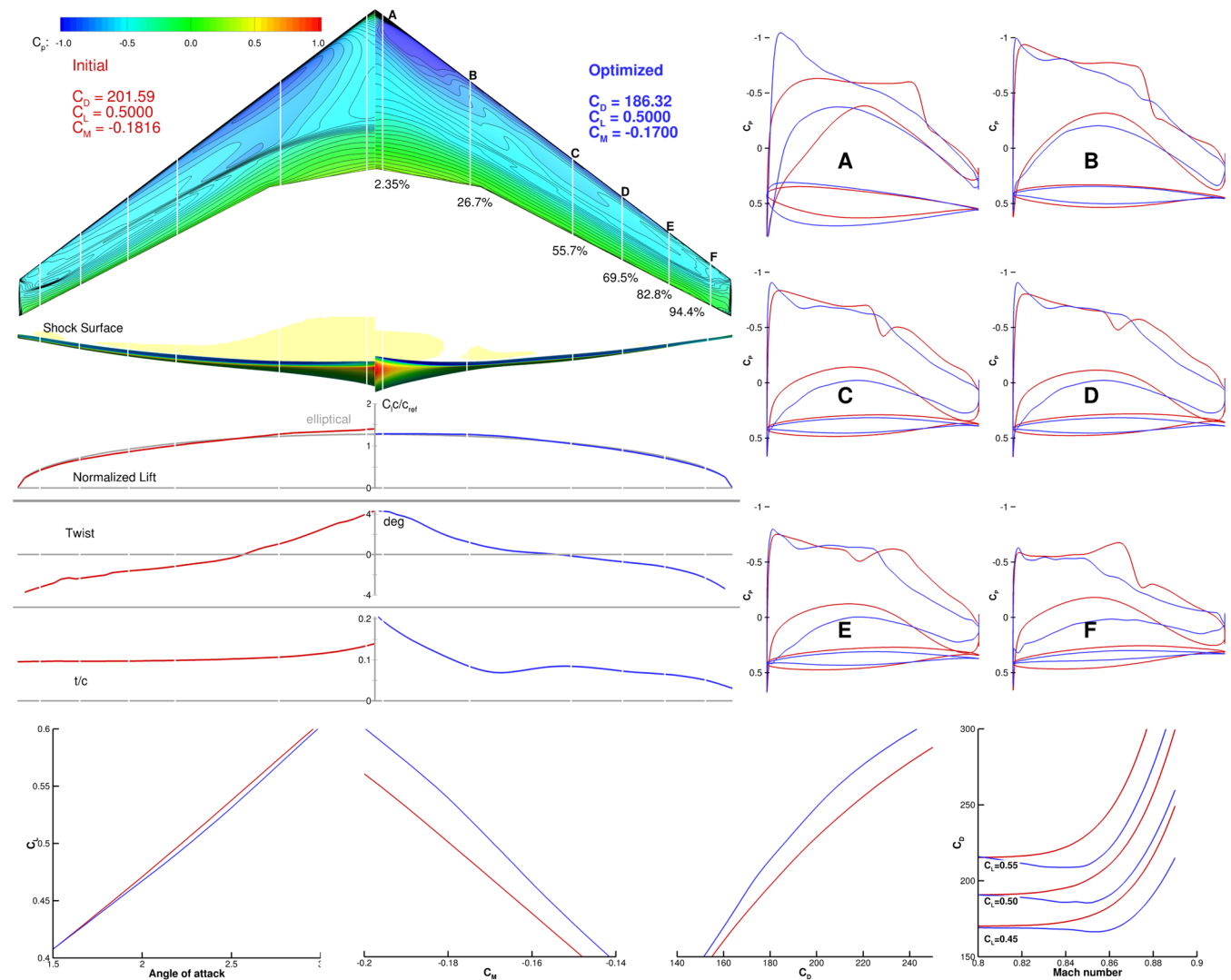


Fig. 8 Case 4.2 has a weak shock at the on-design condition and flatter drag divergence curves.

The coarse grid (L2) optimization problem statements are similar, except that there are only 192 FFD control points. The design variables correspond to those stipulated by the ADODG description. The shape design variables in our case are the z -coordinate displacements of the FFD volume control points, i.e., these points are allowed to move only in the vertical direction. In addition, each operating condition has an independent angle-of-attack variable. Equality constraints for the lift coefficient are enforced at each operating condition. A single pitching moment inequality constraint is enforced only at the nominal flight condition ($M = 0.85$, $C_L = 0.5$) for each optimization.

Finally, two types of geometric constraints are imposed: the internal volume of the wing must be greater than or equal to the initial volume, and the thickness of the wing must be greater than or equal to 25% of the initial thickness at any point. We approximate the wing internal volume by discretely adding the volume from a grid of 24×29 hexahedral volumes distributed from the 1 to 99% chord locations for which the nodes are projected onto the wing upper and lower surfaces. We compute the thickness constraints in a similar manner: a grid of 25×30 nodes from the 1 to 99% local chord locations are projected vertically onto the upper and lower surfaces. The length of each line segment is then constrained to be greater than 25% of the initial length.

IV. Results

A. Multilevel Optimization

In an effort to reduce the overall computational cost of performing the multipoint optimizations, we employ the multilevel optimization

approach described previously by Lyu and Martins [17]. Thus, we first optimize with a coarse mesh and then use the coarse result as a starting point for the optimization based on a finer grid. This is analogous to the grid sequencing startup technique often employed in CFD solvers. Because of the much lower cost of optimizing on the coarse grid, we can afford to do more iterations on this grid. For this approach to be effective, the coarse grid must capture the main characteristics of the flow. For the shape design optimizations presented in this paper, this means capturing the shock strength and location, as well as quantifying the drag reduction that is possible by increasing the root thickness and decreasing the tip thickness.

A comparison of the initial and optimized designs for Case 4.1 is shown in Fig. 5. The first row shows the initial and optimized designs using the L2 grid. The second row shows the L1 optimization using the L2 optimized shape as the starting point. Slices of the airfoil shapes and the corresponding C_p distributions are shown for six spanwise locations on the right side of the figure. We see that the coarse optimization (using the L2 grid) successfully eliminates the shock on the upper wing surface, resulting in parallel isobars. Even without further optimization, almost all of the drag improvement predicted by the coarse grid is realized on the fine grid. Comparing the lines on the C_p distributions, we see that the only significant difference is the appearance of a weak shock on the refined grid. The fine optimization further improves the design, eliminating this shock and lowering the drag even further. This behavior is consistent with previous results, where three grid levels were used [17]. We employ this multilevel approach for all the optimizations in this paper.

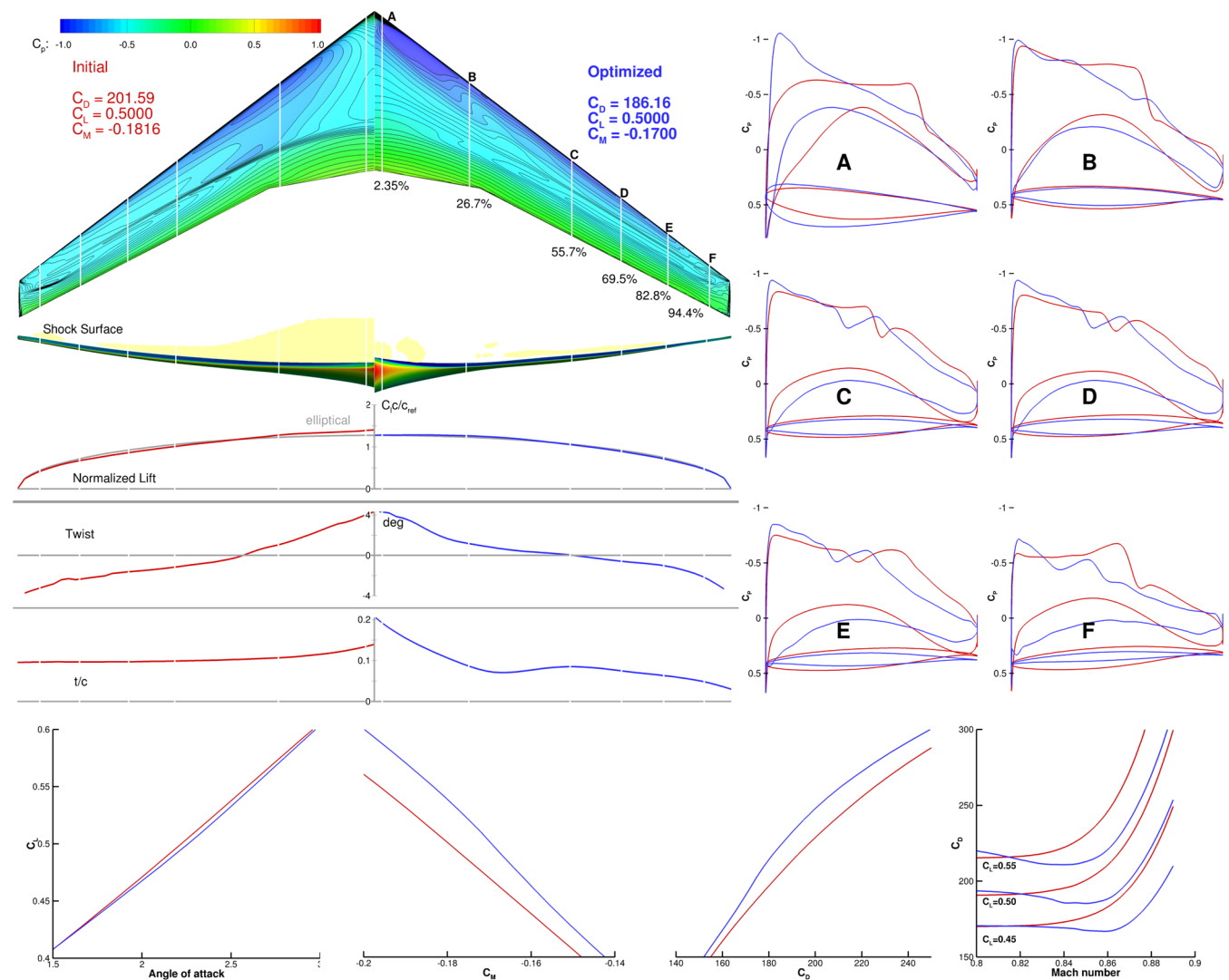


Fig. 9 Case 4.3, which is similar to Case 4.2, exhibits a weak on-design shock.

B. Optimization Results

In this section, we present the main results for the seven CRM wing cases summarized in Table 2. Figure 6 shows the evolution of the SNOPT merit function and optimality. The merit function is used in the augmented Lagrangian formulation, and the optimality is a measure of how well the Karush–Kuhn–Tucker conditions are satisfied [27].

The lift, moment, thickness, and volume constraints are all satisfied to a tolerance of 1×10^{-5} at the end of each optimization. A 200-iteration limit was imposed for the coarse-grid optimizations, resulting in two to three orders of magnitude reduction in the optimality. For the L1 optimizations, a fixed limit of 75 iterations was imposed, resulting in another one to two orders of magnitude reduction in the tolerance. For most of the optimizations, the final tolerance of the L1 optimization is the same order of magnitude as the L2 optimality but, on average, slightly higher. There may be a small improvement that could be made in the fine-grid optimizations, but we feel they are sufficiently converged for the purposes of comparison between the optimized designs.

Figures 7–13 show a summary of the key features of each optimization. The initial configuration results are shown with the optimized results, except for Fig. 13, which compares Cases 4.6 and 4.7. The planform view of the wing shows the C_p contours of the initial geometry (left) and the optimized geometry (right) at the nominal operating condition, along with the corresponding drag coefficients. Just below the planform view, the front view also shows the C_p contours and adds a visualization of the shock surface [30], as well as the physical thickness variation in the wing. Below this, we

plot the spanwise lift, twist, and thickness-to-chord ratio (t/c) distributions. A reference elliptic lift distribution is shown in gray. The right side of the figure displays the cross-sectional shape and C_p distribution at the six spanwise locations stipulated in the ADODG case description. The leftmost three plots on the bottom of the figure show the polar resulting from an alpha sweep at the nominal Mach number of 0.85. The lift, drag, and moment curves corresponding to this alpha sweep are displayed. Finally, the bottom-right plot shows the drag divergence behavior for three lift coefficients: $C_L = (0.45, 0.50, 0.55)$.

There are a few overall trends that are common to all seven optimized results shown in Fig. 7–13. One of these trends is that all the designs result in a significant increase in the t/c near the root, and a large reduction in t/c near the tip. We have previously noticed this behavior for Case 4.1 [17], and the same design tradeoff takes place for the multipoint cases as well. Due to the minimum volume constraint, and the fact that the drag increases with t/c , it is better to have the higher values of t/c inboard of the Yehudi break, where the chords are larger, and thus the trade between viscous pressure drag and volume is more favorable. Another way of looking at this tradeoff is that a wing with higher t/c inboard results in a smaller frontal area for a given volume than a wing with constant t/c .

Overall, there is no significant change in the twist between the initial design and any of the optimized designs. As expected, the optimized lift distribution for Case 4.1 is an elliptic distribution, which yields the lowest induced drag. The optimizations with closely spaced Mach numbers, Cases 4.2 and 4.3, also have lift distributions that are close to elliptical. The remaining widely spaced

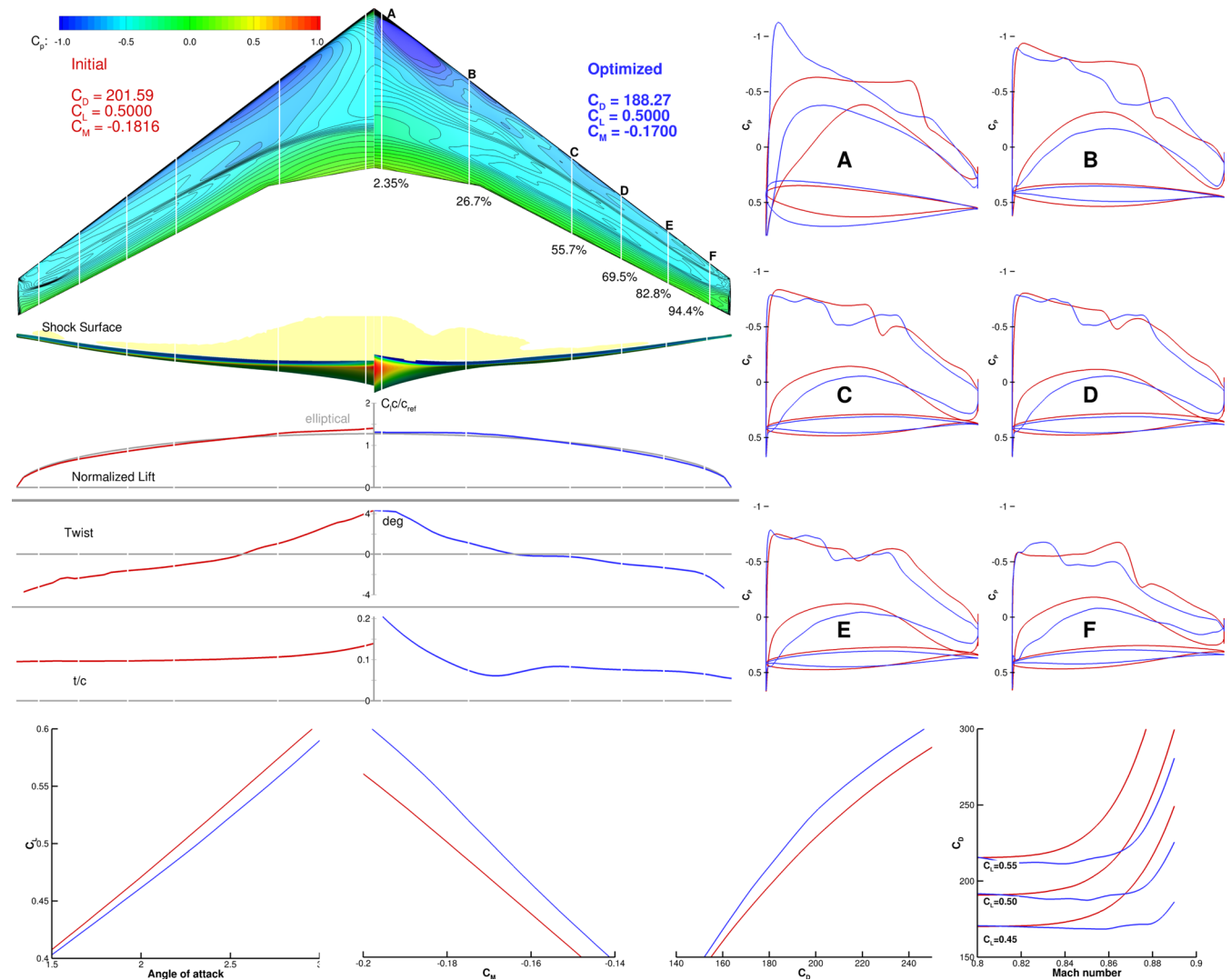


Fig. 10 Case 4.4 has stronger shocks at the on-design condition; the drag divergence curves show multiple dips near the selected operating conditions.

optimizations have a slightly less elliptical distribution, but they are still closer to elliptical than that of the initial design.

The shock surface visualization highlights some of the tradeoffs the optimization is making. Cases 4.2 and 4.3 exhibit weak shocks at the design condition. For the remaining cases, stronger shocks are present at the nominal design condition. Shocks can be seen in all the cases except Case 4.1, which is an expected result of a single-point optimization. The effect of the aforementioned t/c reduction can be clearly seen in the airfoils, especially in airfoils E and F. The optimization has thinned out the airfoils at the tip, especially at the leading edge. This effect is slightly less pronounced in the multipoint designs. This characteristic is highly undesirable from a practical design perspective because of poor low-speed $C_{L_{\max}}$ performance and increased structural weight or possible structural infeasibility.

The preceding discussion has focused on the large-scale changes to the design. In addition to these common changes, the optimizer has made changes on a much smaller scale to improve the local flow characteristics. One issue with the initial CRM geometry is that there is a small amount of trailing-edge flow separation on the outboard span of the wing at the nominal flight condition. This was done by design to provide an additional challenge for the Drag Prediction Workshop [31]. Through very small shape modifications near the trailing edge, the optimization is able to completely eliminate this flow separation from the nominal operating condition for all seven optimizations. This change is shown in Fig. 14 for Case 4.1. This

demonstrates that our RANS model is able to account for the complex turbulent boundary-layer interactions near the trailing edge and that the numerical optimization can fix local issues in the pursuit of the minimization of total drag.

The drag divergence curves for the optimized designs yield interesting trends. The single-point optimized design has a significant drop in C_D around the nominal operating condition. This design does not take into account nearby operating conditions, so C_D is hindered for off-design conditions. This undesirable characteristic is the motivation for multipoint optimization. All of the multipoint optimizations show considerably better off-design performance.

Even with multipoint optimization, it is possible to see the effects of a particular operating condition. Case 4.5 and, to a lesser extent, Case 4.4 show this clearly. There are three distinct dips in the $C_L = 0.5$ drag curve for Case 4.5 at $Mach = (0.82, 0.85, 0.88)$, which coincide with the selected design Mach numbers. The drag divergence curves for the closely spaced design points (Cases 4.2 and 4.3) do not show this effect as dramatically. However, the drag divergence curves are lowered over a narrower range. Finally, Cases 4.6 and 4.7 show a uniform reduction in the drag over the three lift coefficients and over the full range of Mach numbers.

Although drag coefficient divergence curves can yield useful insight into a particular optimized design, it is instructive to examine the contours of ML/cD as well. This is a two-dimensional extension of the drag divergence curves but with an important distinction. In the context of commercial transonic wing design, it is not the actual

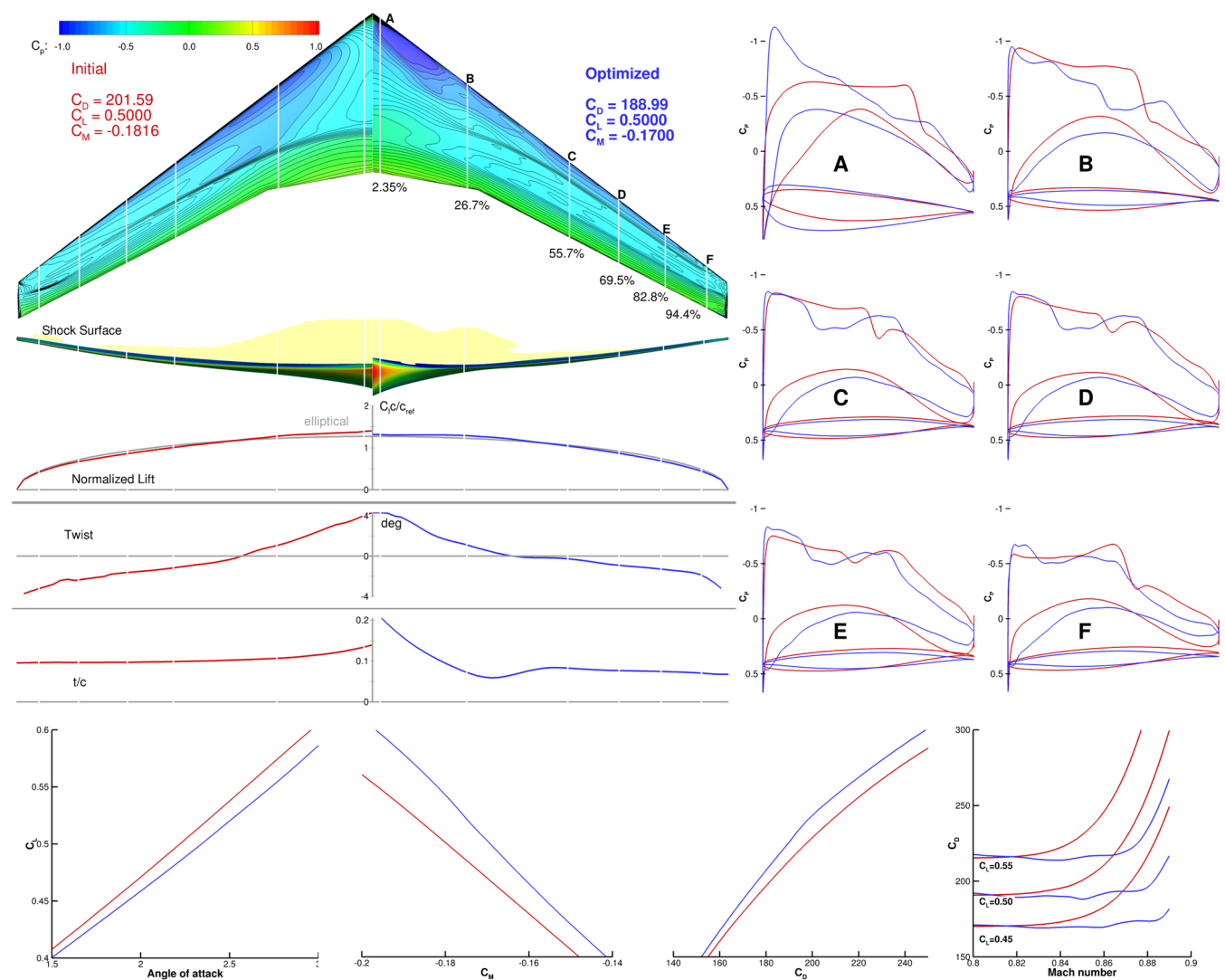


Fig. 11 Case 4.5 result, which is similar to Case 4.4; stronger shocks are present at the on-design condition.

maximum value of L/D that is important but rather the range factor in the Breguet range equation:

$$R = \frac{L}{D} \frac{V}{c} \ln \left(\frac{W_1}{W_2} \right) \quad (1)$$

where L/D is the lift-to-drag ratio, V is the velocity, c is the thrust-specific fuel consumption, and W_1 and W_2 are the initial and final cruise weights, respectively. The range factor is $L/D V/c$. We make the assumption that the speed of sound is constant, which is a good approximation for the typical cruise altitudes of modern airliners. With this assumption, the velocity may be replaced by the Mach number. For the thrust-specific fuel consumption, we use a zero-dimensional engine model to estimate the thrust and thrust-specific fuel consumption for a high-bypass-ratio turbofan similar to a GE-90. The variation of the thrust-specific fuel consumption as a function of Mach number and thrust at an altitude of 37,000 ft is shown in Fig. 15. With fixed W_1/W_2 , ML/cD may be used as a surrogate for the aircraft range.

We evaluate a two-dimensional grid of samples in $M - C_L$ space. Once the drag value is known, we can determine the required thrust and the corresponding thrust-specific fuel consumption. Note that the drag associated with the fuselage, horizontal stabilizer, vertical stabilizer, and pylons is not included, contributing to an underestimation of the drag. On the other hand, the wing-only geometry

has a lower effective span than the full configuration, and our computations use the wind-tunnel test Reynolds number (5 million) instead of the flight Reynolds number (around 40 million), which contributes to an overestimate of the wing drag. Therefore, the values shown in these contours do not correspond to the real aircraft. However, since the various optimization cases are consistent, these contours are adequate for performing a qualitative comparison between the different optimization formulations.

A comparison of the ML/cD contours for the initial and optimized designs is shown in Fig. 16. Two contour values are highlighted: The contour that corresponds to 99% of the maximum value of the initial design and the contour that is the 99% contour of the optimization's own maximum value are shown. The motivation for plotting these 99% contours is that airliners typically fly between the Mach number, yielding maximum range (approximated by the maximum ML/cD value in the figures) and a higher Mach number that yields a 1% fuel-burn drag penalty but a decrease in the flight time. In addition, the area enclosed by the 99% contour is a measure of robustness for a given design: Any $M - C_L$ combination within the contour incurs no more than a 1% fuel-burn penalty.

The performance differences resulting from the different optimizations are now evident. The sharp drag dip for Case 4.1 appears as a small and narrow 99% contour around the nominal operating condition. For this case, the area enclosed by the 37.63 contour is

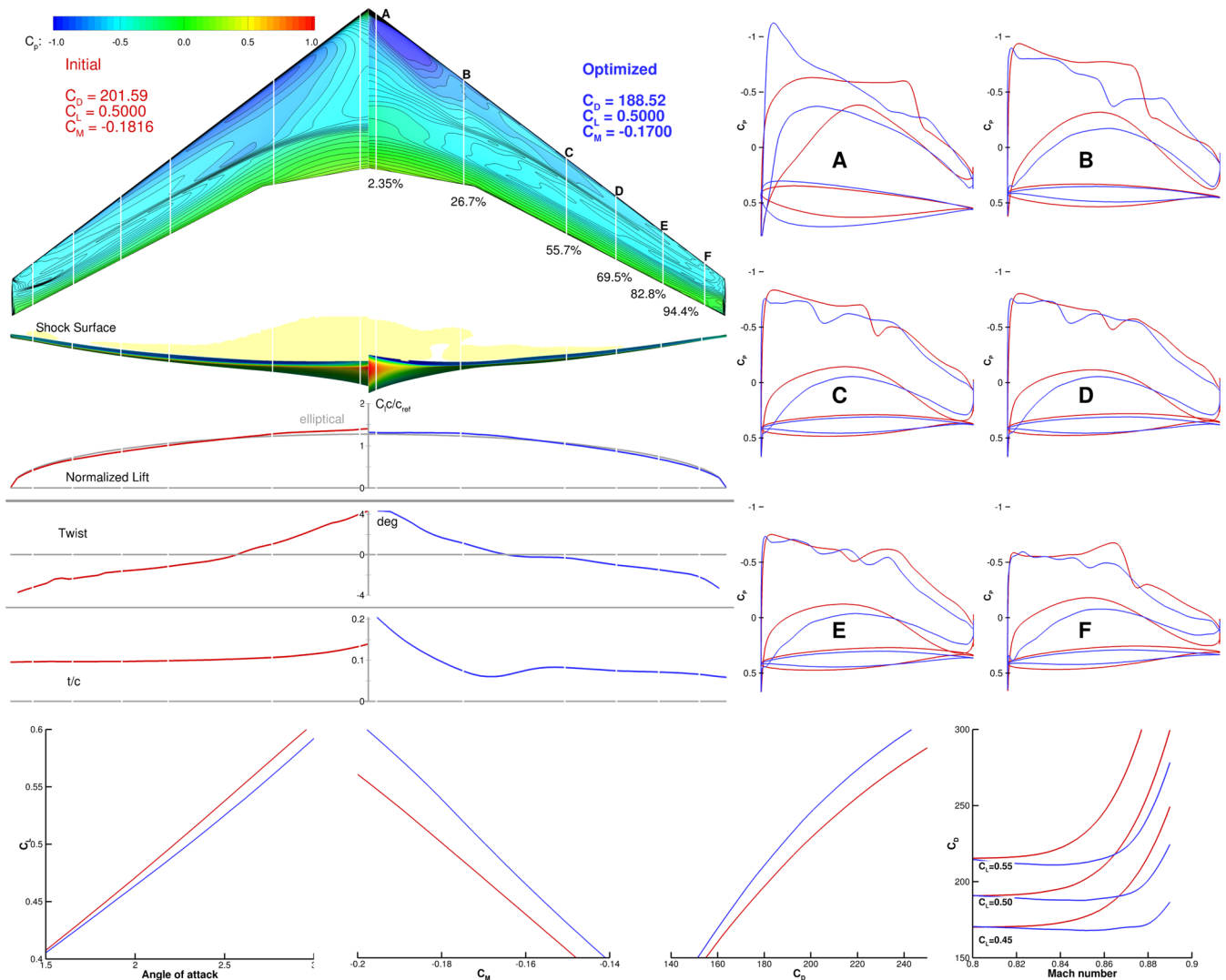


Fig. 12 Case 4.6 has stronger on-design shock waves; however, the drag divergence curve shows more consistent behavior over a wider range of Mach numbers.

approximately the same as in the initial design, although it has been shifted to an overall higher Mach number. As expected, the absolute maximum ML/cD value is obtained by the single-point optimized design (Case 4.1). The next highest values are from the closely spaced design point optimizations (Cases 4.2 and 4.3). For a reduction of less than 0.6% in maximum ML/cD , a significantly enlarged 99% contour is obtained.

We can also see how the choice of design points influences the shape of the resulting contours. The three C_L values at fixed Mach numbers in Case 4.2 result in a narrower and taller 99% contour than for Case 4.3, which is wider and shorter, closely matching the selected operating conditions. For conciseness, we plot only Case 4.5, but Case 4.4 exhibits similar characteristics. In this case, a multimodal operating envelope emerges, as the 99% contour exhibits two distinct regions. One region, containing the overall maximum, is near the nominal operating condition. The second is a small high-performance region near the high-Mach-number design point. Case 4.5 has the lowest maximum of the optimized designs, presumably due to difficulties in reducing the drag at the high-Mach-number operating condition.

The nine-point optimization (Case 4.6), despite containing the same three operating conditions as Case 4.5, has much more robust behavior. Although this design does have the second lowest maximum value, it is the most robust of the optimized designs when considering the area enclosed by the 99% contour, and this contour is fairly close in size to the 99% contour of the initial design. The five-

point optimization (Case 4.7) produces an equally robust design as Case 4.6, but it uses about 55% of the computational resources.

Figure 17 shows that all the optimized designs are markedly less robust than the initial design, as indicated by the size of the 99% contour. However, the nine-point design of Case 4.6 and the five-point design of Case 4.7 achieve a robustness that is almost as good as that of the initial design. Furthermore, these optimizations achieve this performance at a Mach number much closer to the desired nominal value.

Although the optimal design for Cases 4.6 and 4.7 appears to be robust, the comparison in Fig. 17 is not entirely fair, since the maximum value for Case 4.6 is only 99.08% of the maximum value of Case 4.2. For a more appropriate comparison, we compare the 99% contour value from Case 4.6 (ML/cD maximum of 39.11) for all the optimized designs. This is shown in Fig. 18. The optimizations with closely spaced flight conditions (Cases 4.2 and 4.3) now compare much more favorably with the nine-point optimization. Case 4.2, which includes three C_L values at the same Mach number, appears to be more effective than the case with three different Mach numbers at the same C_L . Unsurprisingly, only the cases that include design points at the $M = 0.88$ operating condition (Cases 4.4 through 4.7) show consistently good performance up to and including $M = 0.88$.

From this set of optimization problems, we can draw a few general conclusions with respect to the number and distribution of the operating conditions. It is clear that the single-point optimization results in a design with poor robustness with a higher peak perfor-

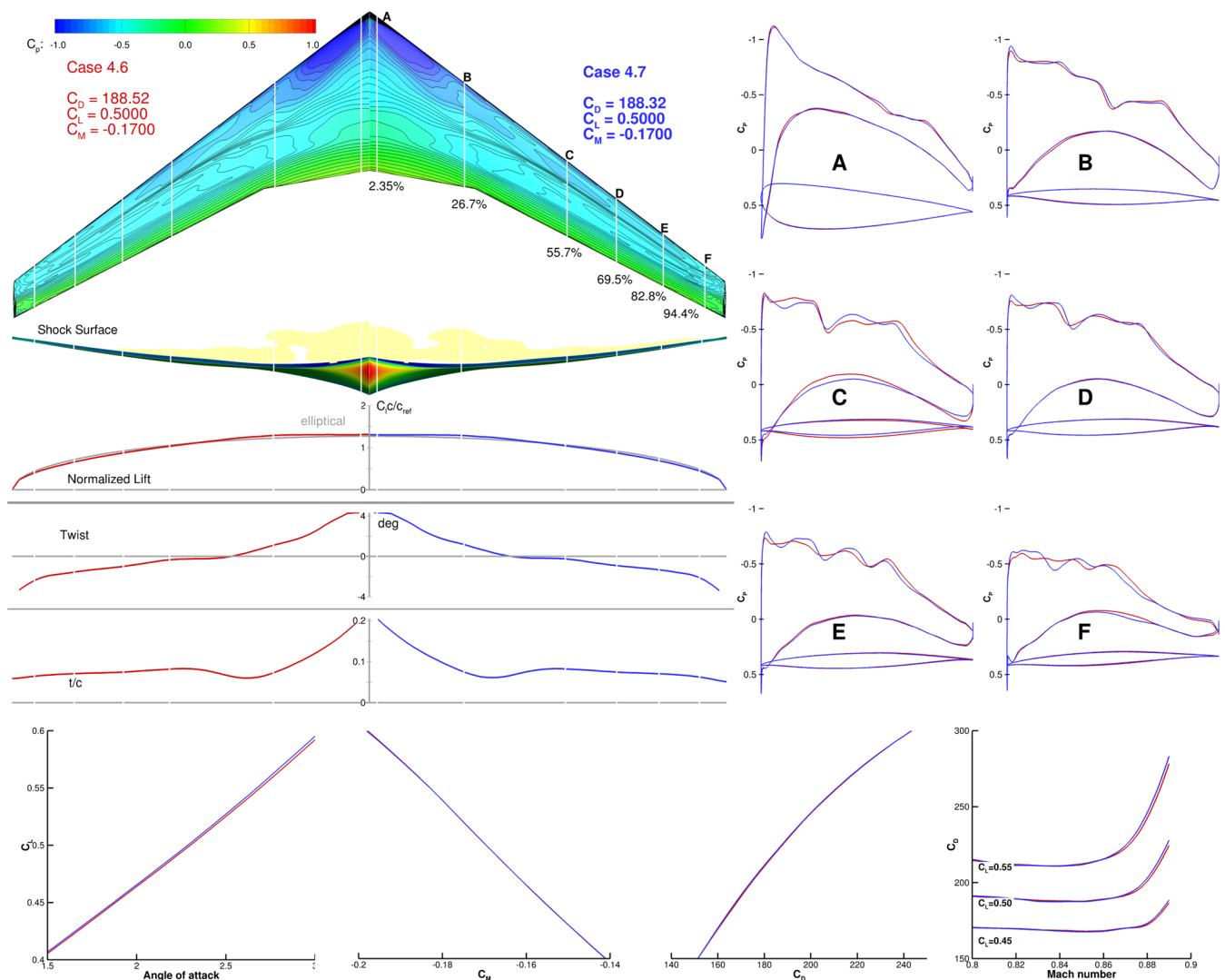


Fig. 13 Cases 4.6 and 4.7 yield similar characteristics, especially for the inboard wing sections

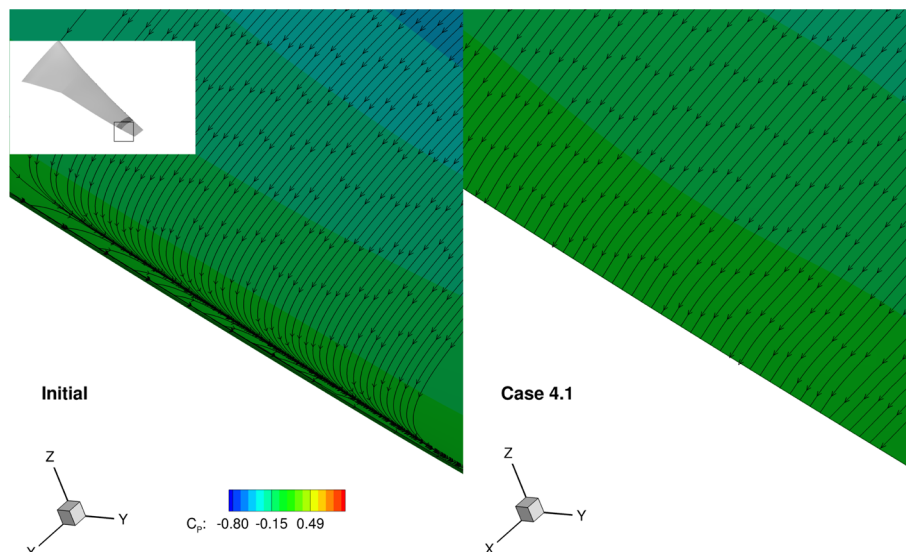


Fig. 14 Shape optimization eliminates the trailing-edge flow separation present in the original CRM wing.

mance. All the three-point optimizations remedied this situation with the widely spaced flight conditions (Cases 4.4 and 4.5), yielding larger 99% contours (although the multimodal performance is undesirable). At least five design flight conditions forming a cross in $M - C_L$ space are required to produce a robust design. However, if a smaller operational envelope is acceptable, as defined by Cases 4.2 and 4.3, three more closely spaced flight conditions may be sufficient. The nine-point optimization (Case 4.6) yields the most robust result, but it incurs the largest computational cost. The five-point optimization (Case 4.7) is the best compromise: With four fewer design points, we can obtain a design with slightly higher peak performance and practically the same off-design performance.

We must caution, however, that all these optimization cases are of only academic interest and are not representative of real aerodynamic shape optimization for an actual transonic aircraft configuration for several reasons. First, the lack of the fuselage results in an incorrect lift distribution. In fact, the lift distribution of the initial CRM combined with the fuselage is closer to elliptic than that of the wing alone without the fuselage [11,32]. Second, the analysis is performed at a wind-tunnel Reynolds number of 5 million, as opposed to the flight Reynolds number of about 40 million. It is currently not known what effect this would have on the optimal design. Third, the 25%

lower bound on the thickness constraints is impractical. In reality, an internal structure would be required to support the wing loads, and the optimized thickness distributions would result in structural issues. In addition, an aircraft wing is not rigid and deforms according to the actual flight loads. This bends and twists the wing, resulting in a different spanwise lift distribution, shock structure, and induced drag. Previous work has addressed the shortcomings of these aerodynamic-only optimizations via aerostructural optimization [9–11,33], but this is currently beyond the scope of the ADODG benchmarks.

We have shown through this series of optimizations that a multipoint formulation with at least three points is necessary for robust off-design performance. Note that, in this paper, “off-design” refers to flight conditions that are different from the nominal condition but still within the nominal operating envelope. However, there are a number of truly off-design conditions that are not meant to occur in normal flight operations. One example is the buffet onset margin: a 1.3 g margin relative to the first perception of buffeting that determines the range of Mach numbers and lift coefficients at which the aircraft may be safely operated. Recent work by the authors has shown that this is an important consideration for transonic wing design optimization [34]. Other off-design performance considerations include the L/D at intermediate Mach numbers for climb performance, as well as the low-speed $C_{L_{max}}$ of the wing, both with and without the high-lift system deployed.

When examining the results of the present work, a natural question arises: Which set of flight conditions and associated weighing constants best represent the actual performance we want to maximize? We did not attempt to completely answer this question here but instead compared the results from various multipoint formulations that are based on intuition. To answer this question, we must first decide what is the true objective function. In aircraft design, the actual objective is a combination of takeoff weight (which includes the fuel weight and structural weight) and fuel burn [35]. When considering the aircraft performance, we would ideally consider all the missions flown by the aircraft accounting for the frequency of each mission and minimize the objective function evaluated for all those missions. To this end, Liem et al. [10] developed a method for finding the flight conditions and corresponding weighing constants based on actual mission data.

C. Computational Cost

Multipoint three-dimensional RANS-based aerodynamic shape optimizations are costly from a computational perspective, and we make every effort to reduce the total cost of the optimizations. Table 4 lists the total CPU cost, in processor hours, required to generate the results presented in this paper. All the computations were performed on the Stampede Compute Cluster at the University of Texas [36].

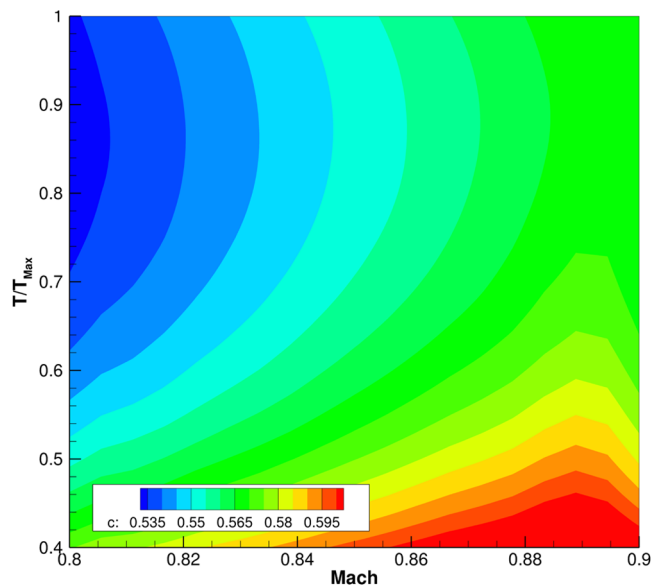


Fig. 15 Thrust-specific fuel consumption (c) contours given by the engine model.

Each computational node consists of two Intel E5-2680 CPUs running at 2.7 GHz with 32 GB of DDR3-1600 MHz RAM. The nodes are connected with FDR InfiniBand. The analyses for the L2 grid used 16 cores (one node) for each flight condition, whereas the analyses for the L1 grid used 64 cores (four nodes) for each flight condition.

Approximately 60% of the total computational cost is allocated to the optimizations, and the remainder is used for postprocessing. The ML/cD contour plots are particularly costly, since each requires 399 individual CFD evaluations. These are evaluated by performing 19 angle-of-attack sweeps for different Mach numbers, each with 21 angle-of-attack values. Since successive angles of attack are close

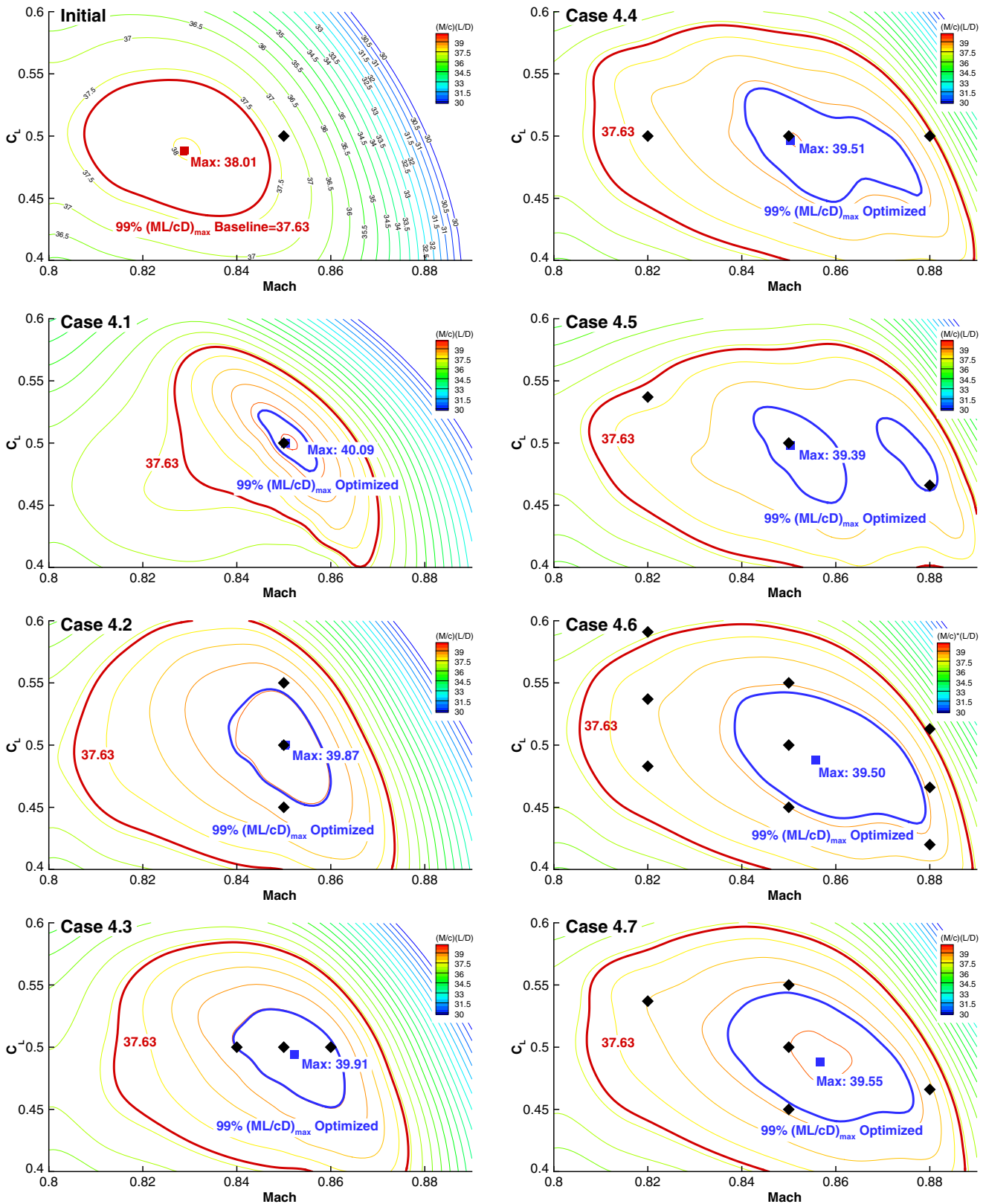


Fig. 16 ML/cD contours for the initial and optimized geometries, where the contour lines are spaced at 0.5 intervals. The maximum is shown by the square, whereas the diamonds represent the flight conditions that were considered.

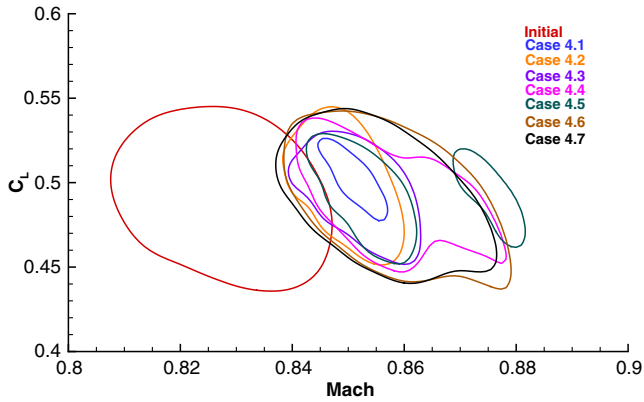


Fig. 17 Contours of $0.99(ML/cD)_{\max}$ for the initial and optimized geometries.

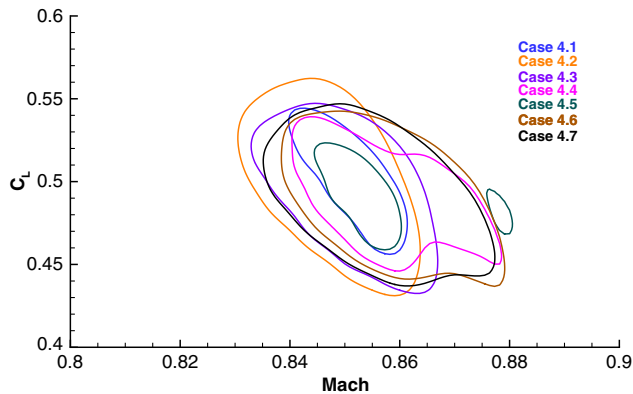


Fig. 18 Contours of $(ML/cD) = 39.11$ for the optimized geometries. The robustness of the closely spaced optimizations (Cases 2 and 3) appear much more favorable for a fixed performance level.

Table 4 Computational cost breakdown in CPU hours

Case	L2 optimization	L1 optimization	Contour	Total
Initial	—	—	2,168	2,168
4.1	93	685	2,168	2,946
4.2	306	2,184	2,168	4,658
4.3	316	2,327	2,168	4,811
4.4	335	2,466	2,168	4,969
4.5	341	2,594	2,168	5,103
4.6	1,093	9,634	2,168	12,895
4.7	652	4,497	2,168	7,317
Total	3,136	24,387	17,344	44,867

together, each solution is started from the solution at the previous angle of attack, so each solution takes substantially less time to converge than a solution from a freestream initial condition.

V. Conclusions

A series of seven optimizations of increasing complexity from the CRM wing shape optimization benchmark defined by the ADODG have been presented. The weighted average drag was minimized with respect to 768 shape design variables, subject to lift, pitching moment, volume, and thickness constraints. A two-level optimization approach was used: a coarse-grid optimization was carried out on a 450,000-cell mesh (L2) with 192 shape variables, followed by a second and final optimization using a 3.6-million-cell mesh (L1) and 768 shape variables.

At the nominal design operating condition of $M = 0.85$ and $C_L = 0.5$, the single-point optimization reduced the drag coefficient by 8.1%, from 201.59 to 185.28 counts. The multipoint optimizations

traded drag improvement at the nominal condition for increased performance over a wider range of operating conditions.

To compare the performance of the optimized designs, we plotted ML/cD in the $M - C_L$ plane. This is a good way to compare wings designed for transonic flow conditions, because it approximates the range factor in the Breguet range equation. The 99% contour of the maximum ML/cD value was used to give an indication of the robustness of each optimized design. The single-point design had the highest range factor, but it was the least robust of the optimized designs. The closely spaced three-point optimizations (Cases 4.2 and 4.3) increased the robustness of the design while lowering the maximum value by less than 0.5%. One of the two widely spaced design point optimizations (Case 4.5) showed two peaks in ML/cD , indicating multimodal performance. In essence, this optimization combined three single-point designs in the same geometric shape. The most robust performance was obtained by the nine-point optimization (Case 4.6). The increased number of operating conditions at different C_L values mitigated the effects of the widely spaced operating conditions of Cases 4.4 and 4.5. The robustness of this design was determined by the area enclosed inside the 99% contour, which compared favorably with that of the initial design. Finally, the additional five-point optimization (Case 4.7) provided the best compromise: The peak performance was higher than the nine-point case and was almost as robust, but it required a much lower computational effort.

Acknowledgments

Funding for this research was provided by NASA under grant number NNX11AI19A. This work used the Extreme Science and Engineering Discovery Environment, which is supported by National Science Foundation grant number ACI-1053575. We would like to thank Justin S. Gray for providing the engine model data.

References

- [1] Pironneau, O., "On Optimum Profiles in Stokes Flow," *Journal of Fluid Mechanics*, Vol. 59, No. 1, 1973, pp. 117–128. doi:10.1017/S002211207300145X
- [2] Jameson, A., "Aerodynamic Design via Control Theory," *Journal of Scientific Computing*, Vol. 3, No. 3, Sept. 1988, pp. 233–260. doi:10.1007/BF01061285
- [3] Nielsen, E. J., and Anderson, W. K., "Aerodynamic Design Optimization on Unstructured Meshes Using the Navier–Stokes Equations," *AIAA Journal*, Vol. 37, No. 11, 1999, pp. 1411–1419. doi:10.2514/2.640
- [4] Anderson, W. K., and Venkatakrishnan, V., "Aerodynamic Design Optimization on Unstructured Grids with a Continuous Adjoint Formulation," *Computers and Fluids*, Vol. 28, No. 4, 1999, pp. 443–480. doi:10.1016/S0045-7930(98)00041-3
- [5] Peter, J. E. V., and Dwight, R. P., "Numerical Sensitivity Analysis for Aerodynamic Optimization: A Survey of Approaches," *Computers and Fluids*, Vol. 39, No. 3, March 2010, pp. 373–391. doi:10.1016/j.compfluid.2009.09.013
- [6] Lyu, Z., Kenway, G. K., and Martins, J. R. R. A., "Aerodynamic Shape Optimization Studies on the Common Research Model Wing Benchmark," *AIAA Journal*, Vol. 53, No. 4, April 2015, pp. 968–985. doi:10.2514/1.J053318
- [7] Mader, C. A., Martins, J. R. R. A., Alonso, J. J., and van der Weide, E., "ADjoint: An Approach for the Rapid Development of Discrete Adjoint Solvers," *AIAA Journal*, Vol. 46, No. 4, April 2008, pp. 863–873. doi:10.2514/1.29123
- [8] Lyu, Z., Kenway, G. K., Paige, C., and Martins, J. R. R. A., "Automatic Differentiation Adjoint of the Reynolds-Averaged Navier–Stokes Equations with a Turbulence Model," *21st AIAA Computational Fluid Dynamics Conference*, AIAA Paper 2013-2581, July 2013. doi:10.2514/6.2013-2581
- [9] Kenway, G. K. W., Kennedy, G. J., and Martins, J. R. R. A., "Scalable Parallel Approach for High-Fidelity Steady-State Aeroelastic Analysis and Derivative Computations," *AIAA Journal*, Vol. 52, No. 5, May 2014, pp. 935–951. doi:10.2514/1.J052255
- [10] Liem, R., Kenway, G. K. W., and Martins, J. R. R. A., "Multimission Aircraft Fuel Burn Minimization via Multipoint Aerostructural

- Optimization," *AIAA Journal*, Vol. 53, No. 1, Jan. 2015, pp. 104–122. doi:10.2514/1.J052940
- [11] Kenway, G. K. W., and Martins, J. R. R. A., "Multipoint High-Fidelity Aerostructural Optimization of a Transport Aircraft Configuration," *Journal of Aircraft*, Vol. 51, No. 1, Jan. 2014, pp. 144–160. doi:10.2514/1.C032150
- [12] Vassberg, J., and Jameson, A., "Influence of Shape Parameterization on Aerodynamic Shape Optimization," von Kármán Inst. for Fluid Dynamics TR, Brussels, April 2014.
- [13] Telidetzki, K., Osusky, L., and Zingg, D. W., "Application of Jetstream to a Suite of Aerodynamic Shape Optimization Problems," *52nd Aerospace Sciences Meeting*, AIAA Paper 2014-0571, Feb. 2014. doi:10.2514/6.2014-0571
- [14] Carrier, G., Destarac, D., Dumont, A., Meheut, M., Din, I. S. E., Peter, J., Khelil, S. B., Brezillon, J., and Pestana, M., "Gradient-Based Aerodynamic Optimization with the elsA Software," *52nd Aerospace Sciences Meeting*, AIAA Paper 2014-0568, Feb. 2014. doi:10.2514/6.2014-0568
- [15] Mader, C. A., and Martins, J. R. R. A., "Stability-Constrained Aerodynamic Shape Optimization of Flying Wings," *Journal of Aircraft*, Vol. 50, No. 5, Sept. 2013, pp. 1431–1449. doi:10.2514/1.C031956
- [16] Mader, C. A., and Martins, J. R. R. A., "Computing Stability Derivatives and Their Gradients for Aerodynamic Shape Optimization," *AIAA Journal*, Vol. 52, No. 11, Nov. 2014, pp. 2533–2546. doi:10.2514/1.J052922
- [17] Lyu, Z., and Martins, J. R. R. A., "Aerodynamic Design Optimization Studies of a Blended-Wing/Body Aircraft," *Journal of Aircraft*, Vol. 51, No. 5, Sept. 2014, pp. 1604–1617. doi:10.2514/1.C032491
- [18] Kenway, G. K. W., Kennedy, G. J., and Martins, J. R. R. A., "Aerostructural Optimization of the Common Research Model Configuration," *15th AIAA/ISSMO Multidisciplinary Analysis and Optimization Conference*, AIAA Paper 2014-3274, June 2014.
- [19] Osusky, L. M., "A Novel Numerical Tool for Aerodynamic Shape Optimization in Turbulent Flow," Ph.D. Thesis, Univ. of Toronto, Toronto, 2013.
- [20] Martins, J. R. R. A., Alonso, J. J., and Reuther, J. J., "High-Fidelity Aerostructural Design Optimization of a Supersonic Business Jet," *Journal of Aircraft*, Vol. 41, No. 3, May 2004, pp. 523–530. doi:10.2514/1.11478
- [21] Kenway, G. K., Kennedy, G. J., and Martins, J. R. R. A., "A CAD-Free Approach to High-Fidelity Aerostructural Optimization," *13th AIAA/ISSMO Multidisciplinary Analysis Optimization Conference*, AIAA Paper 2010-9231, Sept. 2010.
- [22] de Boor, C., *A Practical Guide to Splines*, Springer, New York, 2001, pp. 109–128.
- [23] van der Weide, E., Kalitzin, G., Schluter, J., and Alonso, J. J., "Unsteady Turbomachinery Computations Using Massively Parallel Platforms," *44th AIAA Aerospace Sciences Meeting and Exhibit*, AIAA Paper 2006-0421, 2006.
- [24] Jameson, A., Schmidt, W., and Turkel, E., "Numerical Solution of the Euler Equations by Finite Volume Methods Using Runge-Kutta Time Stepping Schemes," AIAA Paper 1981-1259, 1981.
- [25] Spalart, P., and Allmaras, S., "A One-Equation Turbulence Model for Aerodynamic Flows," *30th Aerospace Sciences Meeting and Exhibit*, AIAA Paper 1992-0439, 1992. doi:10.2514/6.1992-439
- [26] Lyu, Z., Xu, Z., and Martins, J. R. R. A., "Benchmarking Optimization Algorithms for Wing Aerodynamic Design Optimization," *Proceedings of the 8th International Conference on Computational Fluid Dynamics*, ICCFD8-2014-0203, July 2014.
- [27] Gill, P. E., Murray, W., and Saunders, M. A., "SNOPT: An SQP Algorithm for Large-Scale Constrained Optimization," *SIAM Journal on Optimization*, Vol. 12, No. 4, 2002, pp. 979–1006. doi:10.1137/S1052623499350013
- [28] Perez, R. E., Jansen, P. W., and Martins, J. R. R. A., "pyOpt: A Python-Based Object-Oriented Framework for Nonlinear Constrained Optimization," *Structural and Multidisciplinary Optimization*, Vol. 45, No. 1, Jan. 2012, pp. 101–118. doi:10.1007/s00158-011-0666-3
- [29] Chan, W. M., and Steger, J. L., "Enhancements of a Three-Dimensional Hyperbolic Grid Generation Scheme," *Applied Mathematics and Computation*, Vol. 51, Nos. 2–3, 1992, pp. 181–205. doi:10.1016/0096-3003(92)90073-A
- [30] Haimes, R., "Automated Feature Extraction from Transient CFD Simulations," *Proceeding of the 7th Annual Conference of the CFD Society of Canada*, May 1999.
- [31] Vassberg, J., "Introduction: Drag Prediction Workshop," *Journal of Aircraft*, Vol. 45, No. 3, June 2008, pp. 737–737. doi:10.2514/1.37761
- [32] Chen, S., Lyu, Z., Kenway, G. K. W., and Martins, J. R. R. A., "Aerodynamic Shape Optimization of the Common Research Model Wing-Body-Tail Configuration," *AIAA Science and Technology Forum and Exposition (SciTech)*, AIAA Paper 2015-1718, Jan. 2015. doi:10.2514/6.2015-1718
- [33] Kenway, G. K. W., and Martins, J. R. R. A., "Multipoint Aerodynamic Shape Optimization Investigations of the Common Research Model Wing," *AIAA Science and Technology Forum and Exposition (SciTech)*, AIAA Paper 2015-0264, Jan. 2015. doi:10.2514/6.2015-0264
- [34] Kenway, G. W. K., and Martins, J. R. R. A., "High-Fidelity Aerostructural Optimization Considering Buffet Onset," *16th AIAA/ISSMO Multidisciplinary Analysis and Optimization Conference*, AIAA Paper 2015-2790, June 2015.
- [35] Kennedy, G. J., Kenway, G. K. W., and Martins, J. R. R. A., "High Aspect Ratio Wing Design: Optimal Aerostructural Tradeoffs for the Next Generation of Materials," *AIAA Science and Technology Forum and Exposition (SciTech)*, AIAA Paper 2014-0596, Jan. 2014.
- [36] Towns, J., Cockerill, T., Dahan, M., Foster, I., Gaither, K., Grimshaw, A., Hazlewood, V., Lathrop, S., Lifka, D., Peterson, G. D., Roskies, R., Scott, J. R., and Wilkins-Diehr, N., "XSEDE: Accelerating Scientific Discovery," *Computing in Science and Engineering*, Vol. 16, No. 5, Sept. 2014, pp. 62–74. doi:10.1109/MCSE.2014.80

R. Kapania
Associate Editor